MTLA 36 (2024) 102175

Contents lists available at ScienceDirect

Materialia

journal homepage: www.elsevier.com/locate/mtla

Full length article

Strain-field calculation based on X-ray CT images via point matching of impurities using Voronoi diagram

Akio Ishii [a,*], Keitaro Horikawa [a], Masato Hoshino [b], Kentaro Uesugi [b]

[a] Department of Mechanical Science and Bioengineering, Osaka University, 1-3 Machikaneyama-cho, Toyonaka, Osaka 560-8531, Japan
[b] Japan Synchrotron Radiation Research Institute, 1-1-1 Koto Sayo-gun Sayo-cho, Hyogo 679-5198, Japan

ARTICLE INFO

Keywords:
X-ray CT
Strain field
Point matching
Voronoi diagram

ABSTRACT

We propose an approach for calculating the strain field inside materials using X-ray computed tomography (CT) images obtained during deformation tests. Our approach is based on the point matching of the detected impurities from the CT images, and the points in the reference and deformed CT images are used to construct a Voronoi diagram. In addition to the change in distance between the reference and deformed points, the volume and shape of the Voronoi polyhedra at each point are used for point matching. By applying the proposed method to a notched Al alloy sample, we calculated the change in the strain field around the notch during deformation in a tensile test using X-ray CT images, and our method was validated.

1. Introduction

In situ observation of the changes in the internal microstructures of materials during deformation tests is important for understanding the mechanism of plastic deformation of materials and is typically achieved using high-resolution X-ray computed tomography (CT) images owing to the recent development of synchrotron radiation facilities [1–5]. X-ray CT images are also useful for estimating the strain field inside material, and they allow nondestructive onsite observation of the strain field. Digital image correlation (DIC) and digital volume correlation (DVC) are conventional methods for calculating two-dimensional (2D) or three-dimensional (3D) strain fields via CT images by using highly contrasted patterns in the images [6–12]. As another method for calculating the strain field, microstructural feature tracking (MFT), which identifies the individual points of impurities (particles and pores) through direct observation of the volume or surface area of the impurities from the CT image contrast, is also popular [2,13–20]. However, these methods have limitations. Although DIC and DVC are effective for calculating the strain field of a material, their application scope is limited; it is usually difficult to apply them to CT images of the inside of pure materials, because there is often no contrast or low contrast, and it is difficult to select a highly patterned region [21,22]. The shape changes of the impurities in CT images typically affect the results of MFT; some particles and pores may grow during deformation, and in such situations, identification using MFT becomes difficult.

Herein, we propose an approach for calculating the strain field inside materials using the points of impurities detected from X-ray CT images during a deformation test. Our approach is based on matching the detected points, and each point in the reference and deformed CT images is used to construct a Voronoi diagram [23]. In addition to the change in the distance between the reference and deformed points, the volume and shape of the Voronoi polyhedra at each point are used for point matching, because the size and shape of the Voronoi polyhedron reflect the geometric relationship between the points in the matching [23].

2. Methodology

Considering that each point of the impurities in the reference and deformed systems was detected from the CT images using a certain method such as image thresholding [16,17], we implemented point matching between the points in the reference and deformed systems using the Voronoi diagram. Fig. 1 presents a 2D schematic of our method of point matching for calculating the strain field using the Voronoi diagram. The Voronoi polyhedron for a certain point is constructed as an area surrounded by perpendicular bisector planes between other points. For all the points in the reference and deformed systems, the volume (v) and number of faces (f) of each polyhedron were determined using the calculated Voronoi diagram. For point i of the reference and point

* Corresponding author.
E-mail address: ishii@me.es.osaka-u.ac.jp (A. Ishii).

https://doi.org/10.1016/j.mtla.2024.102175
Received 12 April 2024; Accepted 6 July 2024
Available online 9 July 2024

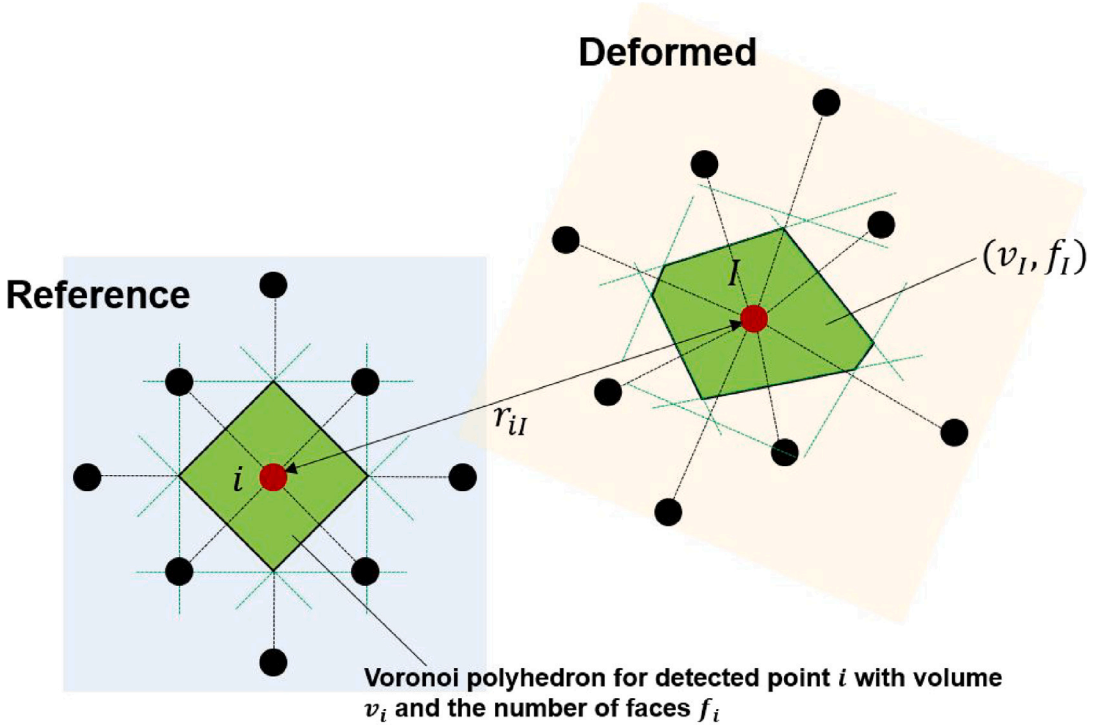

Fig. 1. 2D schematic of the point matching using the Voronoi diagram. The dots indicate the detected points (impurities), and green areas indicate the Voronoi polyhdra for a certain point i (in reference system) and I (in deformed system). The broken lines are for visual guidance to construct the Voronoi diagram; the black ones connect the points in the image, and the green ones are the perpendicular bisectors of the black ones.

I of the deformed system at the cutoff distance r_{cut}, we calculated the matching parameters M_{iI} (ranging from 0.0 to 1.0) as follows:

$$\begin{aligned} M_{iI} &= \frac{\alpha R_{iI} + \beta V_{iI} + \gamma F_{iI}}{\alpha + \beta + \gamma}, \\ R_{iI} &= \frac{r_{\mathrm{cut}} - |\boldsymbol{r}_{iI}|}{r_{\mathrm{cut}}}, \\ V_{iI} &= \frac{v_{\max} - |v_i - v_I|}{v_{\max}}, \\ F_{iI} &= \frac{f_{\max} - |f_i - f_I|}{f_{\max}}. \end{aligned} \tag{1}$$

Here, $|\boldsymbol{r}_{iI}|$ represents the distance between points i and I, which indicates a change in position during deformation. $v_{\max}$ and $f_{\max}$ represent the maximum volume and number of faces, respectively. α, β, and γ are the weight factors used as the setting parameters. For each point i in the reference system, the points with the maximum M_{iI} are selected as the matched pair, and the total numbers of points in the reference and deformed systems are not necessarily the same. We select the volume and number of faces of the Voronoi polyhedron as matching parameters because we believe that the deformation does not change the properties significantly; the shear deformation does not change the volume significantly, and the tension and compression do not change the shape (the polygon) significantly. For example, it has been confirmed that the shape of a Voronoi polyhedron constructed using the positions of atoms does not change significantly for metallic glasses, even during large deformation [24–26], indicating its robustness to deformation. Some readers may consider our method similar to MFT; however, the difference between our method and conventional MFT is that our method focuses on the local geometry of the detected positions of impurities, whereas MFT focuses on the shape of the impurity, for example, the volume or surface area. Thus, the growth of particles or pores, as mentioned in the Introduction, does not affect matching in our method.

After point matching, we calculated the local strain at each point by using the concept of atomic strain [27], where the local strains $\boldsymbol{\varepsilon}_i$ at point i were calculated in the following form of green strain using the local deformation gradient tensor $\boldsymbol{J}_i$:

$$\begin{aligned} \boldsymbol{\varepsilon}_i &= \frac{1}{2}(\boldsymbol{J}_i(\boldsymbol{J}_i)^T - \boldsymbol{E}), \\ \boldsymbol{J}_i &\equiv \left(\sum_{j \in N_i} (\boldsymbol{r}_{ij}^{\mathrm{ref}})^T \boldsymbol{r}_{ij}^{\mathrm{ref}} \right)^{-1} \left(\sum_{j \in N_i} (\boldsymbol{r}_{ij}^{\mathrm{ref}})^T \boldsymbol{r}_{ij}^{\mathrm{def}} \right). \end{aligned} \tag{2}$$

Here, E is an identity matrix, and the superscripts "ref" and "def" denote the reference and deformed systems, respectively. j is another point near i, and N_i represents the total number of points around point i within the cutoff distance r_{cut}. This form of the deformation gradient tensor is determined to minimize the square of the non-affine displacement at point i [27]:

$$D_i^2 = \sum_{j \in N_i} |\boldsymbol{r}_{ij}^{\mathrm{def}} - \boldsymbol{J}_i \boldsymbol{r}_{ij}^{\mathrm{ref}}|^2.$$

3. Parametric study for determination of weight factors using randomly distributed points

Before the practical application of our strain-field calculation method, we applied point matching to the system to confirm its effectiveness and to determine the appropriate weight factors α, β, and γ in Eq. (1). In the $x_1 \times x_2 \times x_3 = 100 \times 100 \times 100$ box-like region, 10000 indexed points were randomly distributed as a reference system. Five reference systems with different distributions were prepared. For all the reference systems, the entire system was affinely deformed to prepare the deformed systems. Uniaxial tension, shear deformation, and both uniaxial tension and shear deformation were applied to the reference systems with strains of 0.01–0.05 in increments of 0.01. By fixing $\alpha = 1.0$ and changing the weight factors β and γ from 0.0 to 2.0, point matching was implemented for the prepared reference and deformed systems, and the matching rate (the rate of correct answers) was evaluated. Voro++ code was used to construct the Voronoi diagram and extract information from the Voronoi polyhdra [28]. r_{cut} was set as 10.

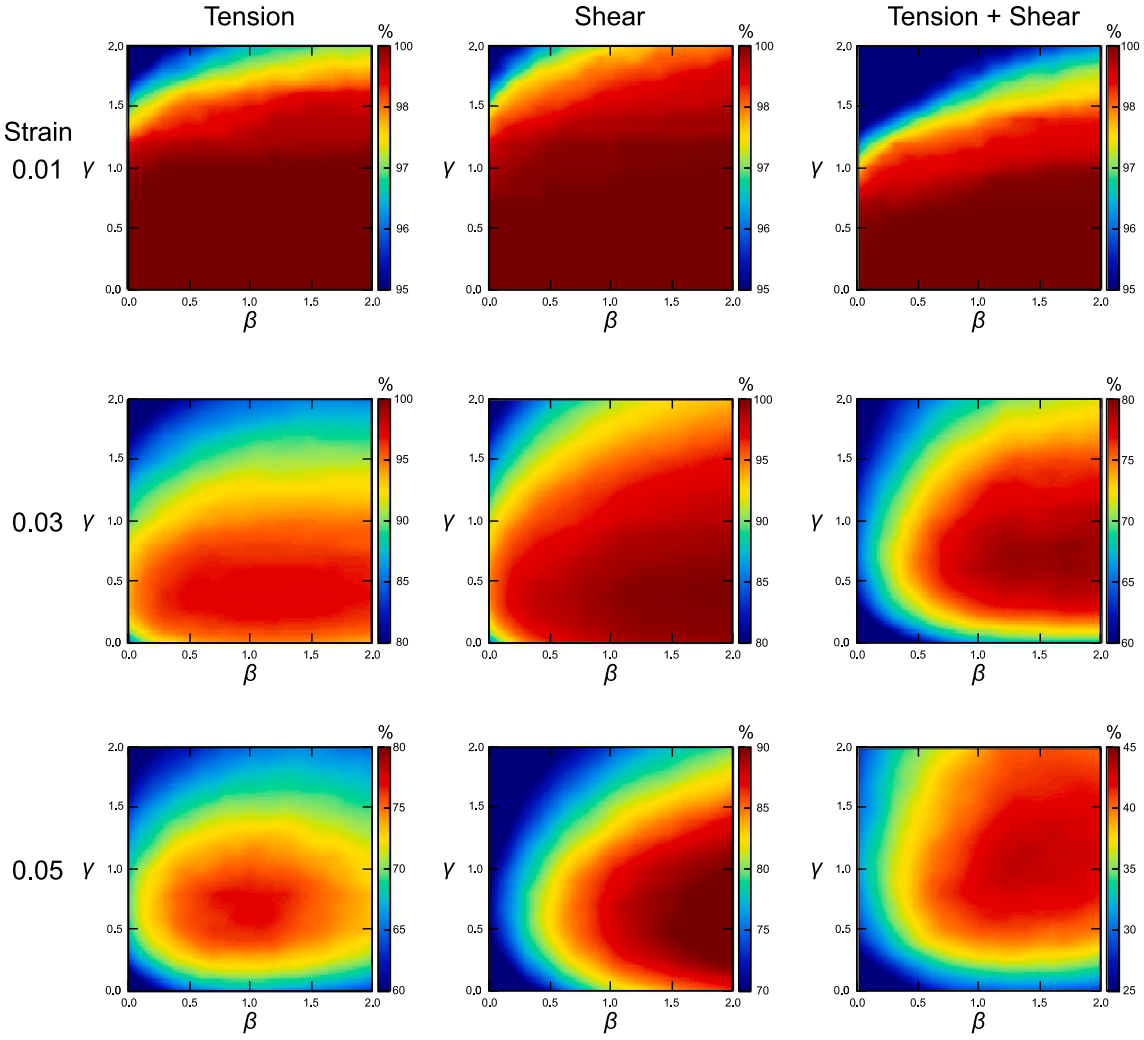

Fig. 2. Matching-rate map with respect to the weight factors β and γ; α is set as 1.0.

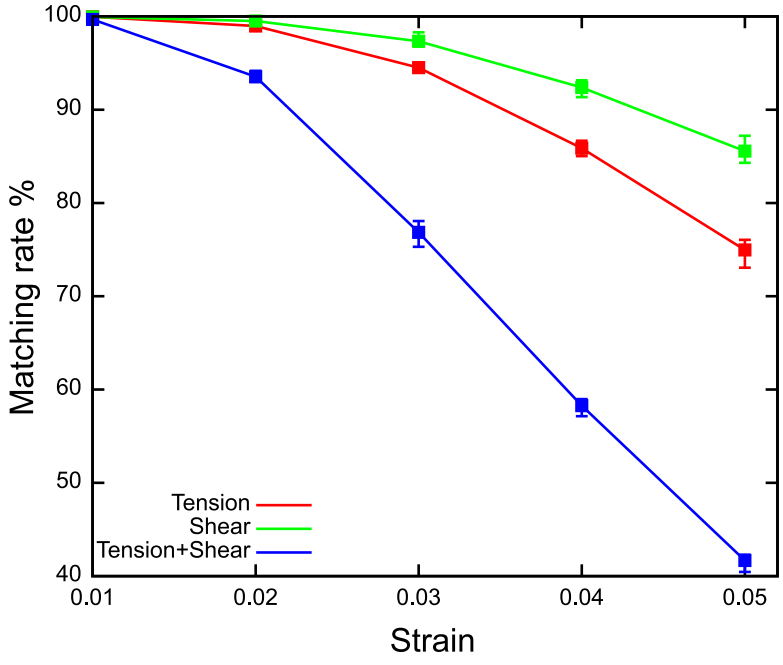

Fig. 3. Strain vs. matching rate plot for $(\alpha, \beta, \gamma) = (1.0, 1.0, 1.0)$.

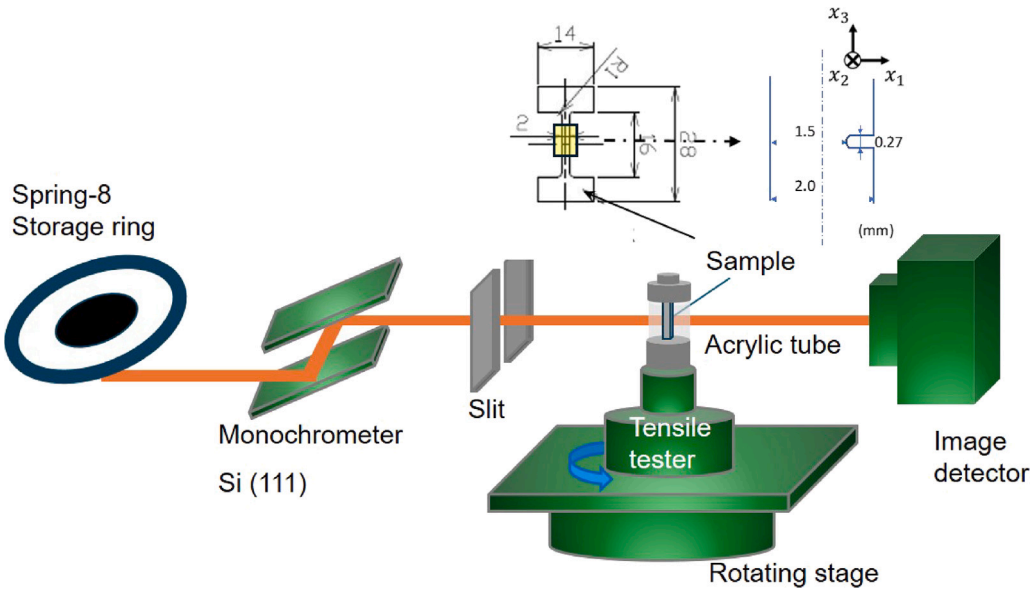

Fig. 4. Setup of synchrotron X-ray microtomography.

Fig. 2 shows the matching-rate map with respect to the weight factor β and γ for a certain initial distribution as an example. Although simple point matching with the distance ($(\beta, \gamma) = (0.0, 0.0)$) is sufficient for the low-strain 0.01 condition, the matching rate appears to increase significantly for higher-strain cases if we select adequate β and γ values. For all the maps investigated, the region with a high matching rate always appears to be around $(\beta, \gamma) = (1.0, 1.0)$, indicating that $(\alpha, \beta, \gamma) = (1.0, 1.0, 1.0)$ is a good choice for the setting parameters. We observed similar trends for other reference systems. Fig. 3 presents strain vs. matching rate plots with error bars for $(\alpha, \beta, \gamma) = (1.0, 1.0, 1.0)$. From this figure, we can confirm that the effect of the distribution of points on the matching rate is insignificant because the ranges of the error bars are very narrow. From Figs. 2 and 3, correct matching appears to be difficult if the strain is too high or complex, although considering the Voronoi properties for the matching increases the matching rate; the matching rate decreases significantly for 0.05 strain and the tension–shear mixed condition. Thus, the sequential matching is recommended for practical applications, although many CT images of the deformation process are necessary; we first performed matching with 0 and 0.01 strain, next with 0.01 and 0.02, and then with 0.02 and 0.03.

4. Strain-field calculation via X-ray CT images for notched sample of Al alloy

4.1. Experimental

After confirming the effectiveness of our point-matching method as described in the previous section, we applied our method to analyze the X-ray CT images captured during the deformation test and calculated the strain fields of the notched sample of the Al alloy during tension. First, we present the experimental settings. Al-5.5% Zn-2.6% Mg-1.6% Cu-0.21% Cr-0.28% Fe-0.21% Si alloy ingots (in mass %) were cast into a copper mold with a thickness of 50 mm. The ingot surface was machined and homogenized at 470 °C for 8 h. After hot and cold rolling, we prepared a plate test specimen with a thickness of 1.0 mm. Plate tensile specimens with gauge lengths of 14.0 mm, widths of 2.0 mm, fillet radii of 1.0 mm, and thicknesses of 1.0 mm were cut from the rolled sheets. The longitudinal direction of the test specimen was transverse to that of the rolled sheet (T-direction). At the center of the gauge part of the tensile specimens, a single U-notch (depth 0.5 mm, minimum diameter of notch bottom 0.27 mm) was made on one side of the specimens. The specimens were solution heat treated at 493 °C for

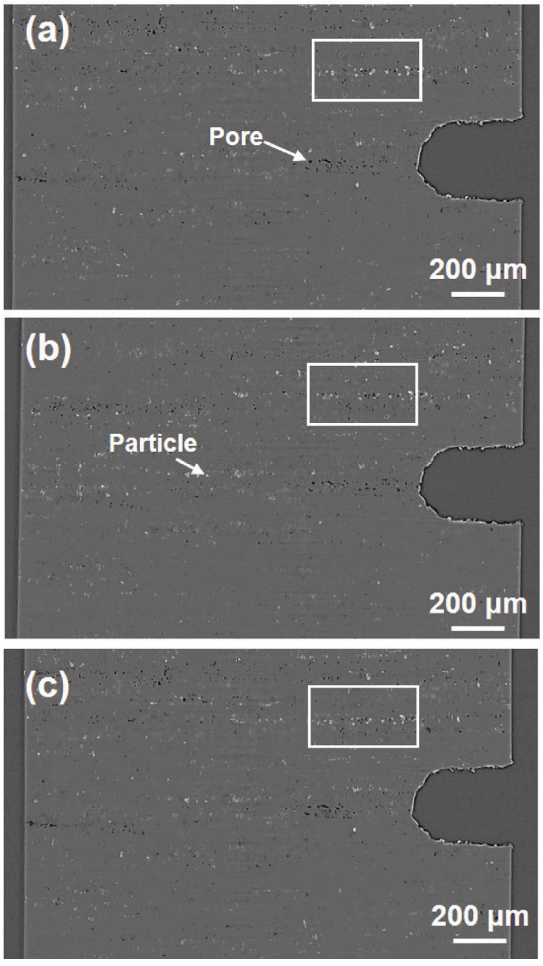

Fig. 5. X-ray CT images of the x_1–x_3 cross section around the notch at the center of the sample: (a) unloading; (b) 400-N loading; (c) 600-N loading. The bright (dark) patterns are considered as particles (pores). White squares indicate the particles and pores shown in Fig. 8.

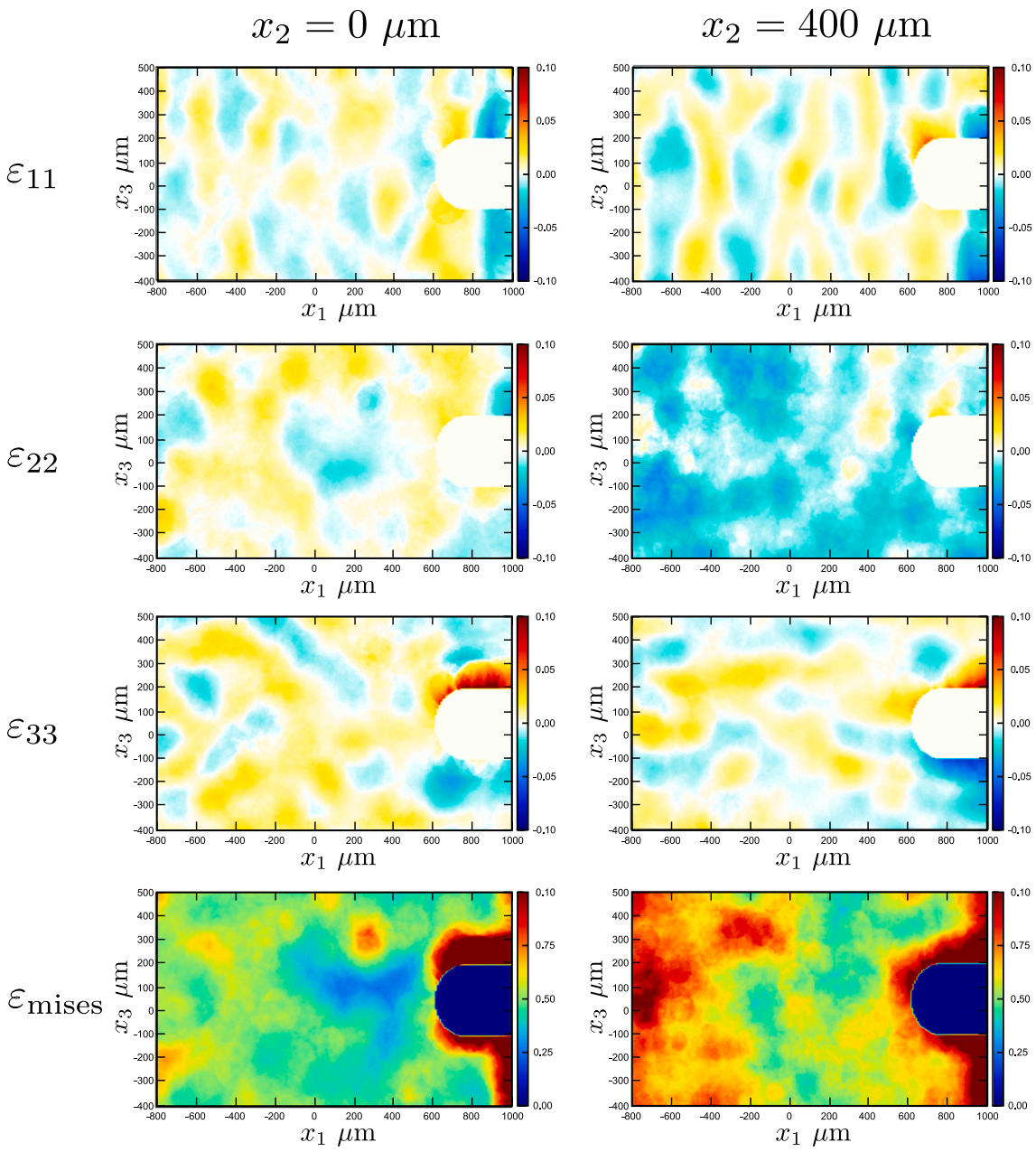

Fig. 6. Strain field around the notch for 400-N uniaxial tension calculated using the detected particles. The origin of the coordinate system is set at the center of mass of all the points.

0.3 h in an air atmosphere; then, they were quenched in water to room temperature and finally aged at 120 °C for 24 h (T6-tempered). The average grain size after heat treatment was 16.3 μm. The interior of the alloy was examined at the high-brightness Japanese synchrotron facility SPring-8 using X-ray μCT (Beamline BL20B2), as shown in Fig. 4. A monochromatic X-ray beam with a photon energy of 40 keV generated by a liquid-nitrogen-cooled Si (111) double-crystal monochromator was used. An image detector consisting of a charge-coupled device (CCD) camera was positioned 90 mm behind the specimen, and 1800 radiographs were obtained. The self-made in situ loading stage allowed the specimens to be subjected to monotonic tensile loading.

First, the unloaded specimens were rotated by 180° on the stage while performing CT imaging (exposure time of 60 ms/frame, 3600 frames/180°). The cross section of the specimen around the U-notch, which had a height of 2021 μm, was captured using a CCD camera. After the observation, tensile deformation with a constant load of 400 or 600 N was applied to the specimens, followed by a second or third CT scan. The image slices were reconstructed using a conventional filtered back-projection algorithm. The gray value in each dataset was calibrated such that a linear absorption coefficient of −13 to 50 cm^{-1} fell within an 8-bit grayscale range of 0–255. All 2D sectional microstructure images were converted into 3D images using the rendering software Amira3D, which is commercially available.

4.2. Results and discussion

Fig. 5 presents the captured 2D CT images of the x_1–x_3 cross section at the center of the sample around the notch for (a) unloading, (b) 400-N, and (c) 600-N tension conditions as an example. Through the thresholding of the rendered 3D CT images from the 2D images in the region ±1.0 mm from the notch along the x_3 direction, 201614, 201916, and 201215 points of the particles (the inclusions due to the alloying) were detected as “bright” patterns for the unloading, 400-N, and 600-N tension conditions, respectively. Each particle position was

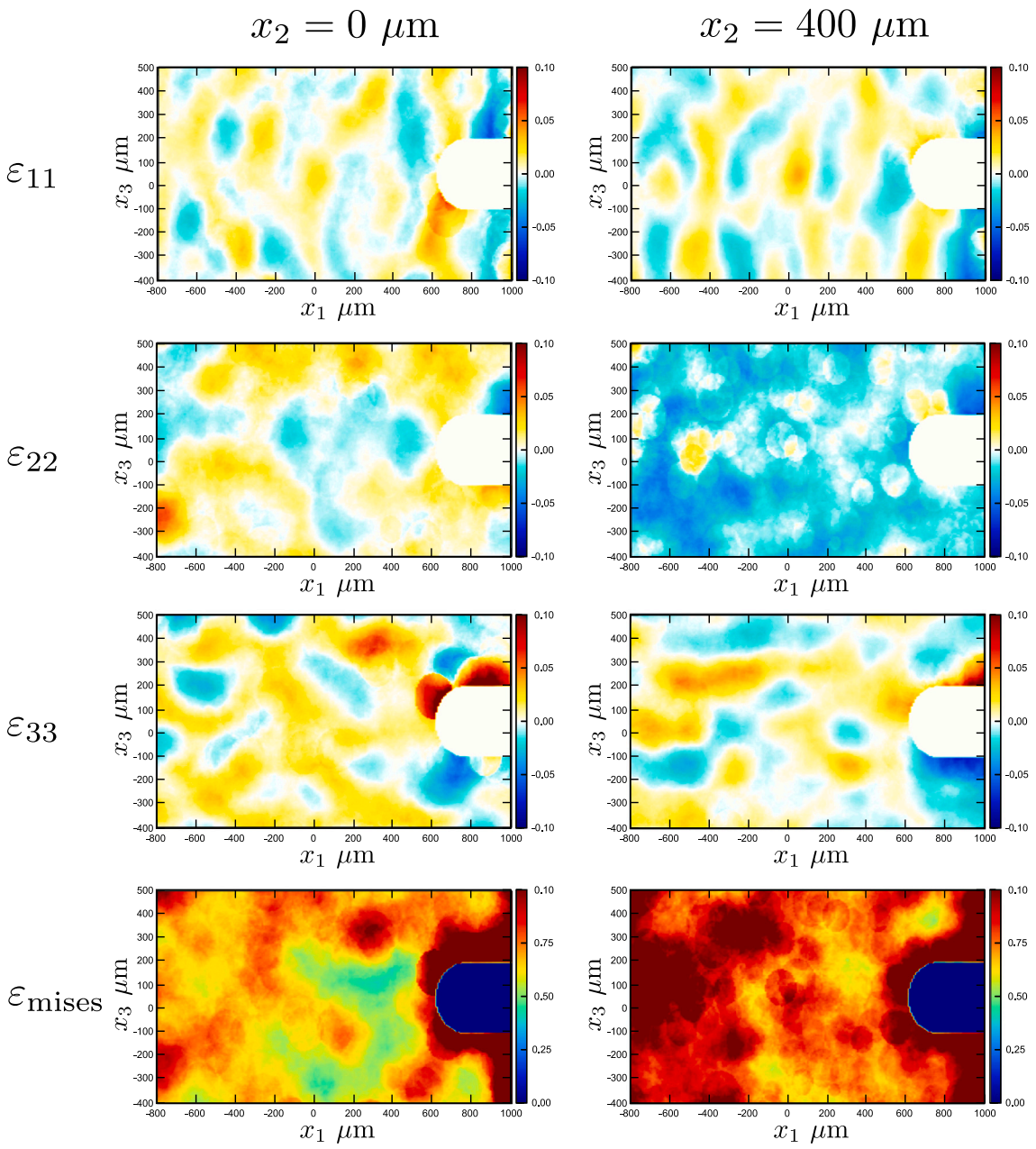

Fig. 7. Calculated strain field around the notch for 600-N uniaxial tension using the detected particles. Note the origin of the coordinate system is set at the center of mass of all the points.

considered the center of corresponding pattern. Then, point matching with setting parameters $(\alpha, \beta, \gamma) = (1.0, 1.0, 1.0)$ was implemented. First, we used the groups of detected points of unloading and 400-N tension as the reference and deformed systems, respectively, and then sequential matching was implemented using 400- and 600-N tension as the reference and deformed systems, respectively. r_{cut} was set as 100 μm; otherwise, we could not find neighbors for several points, indicating that the population of particles in the sample was sparse. After the matching, using Eq. (2), the local strains were calculated for the points with large matching parameters, i.e., $M_{iI} > 0.7$. The average M_{iI} was approximately 0.85 during the matching process. Eventually, grid maps of the strain field were drawn by averaging the values of the local strains of the points around each grid. In Figs. 6 and 7, the calculated strain fields of x_1–x_3 cross section at $x_2 = 0$ μm (the center of the sample) and $x_2 = 400$ μm (near the surface of the sample) planes for 400- and 600-N tension are shown. The origin of the coordinate system is set at the center of mass of all the points. The following Mises strain map is included in addition to the normal strain components, which is a good measurement of the local plastic deformation [27]:

$$\varepsilon_{\mathrm{mises}} \equiv \sqrt{\frac{1}{6}\left((\varepsilon_{11}-\varepsilon_{22})^2+(\varepsilon_{11}-\varepsilon_{33})^2+(\varepsilon_{22}-\varepsilon_{33})^2\right)+\varepsilon_{23}^2+\varepsilon_{31}^2+\varepsilon_{12}^2}.$$

From the calculated strain fields, a high strain concentration, i.e., ε_{33}, around the notch was observed, which increased as the loading increased. The concentration was higher at the center than at the surface. In cases where the plastic deformation is limited near the U-notch, the deformation is constrained by the surrounding elastic portion [29,30]. Even if the specimen is thin, as in the present case, the constraint from the surrounding elastic portion in the center region is strong in the direction of the specimen thickness if the plastic zone dimension at the U-notch tip is sufficiently smaller than these dimensions. In the present case, larger strains were induced at the inner center of the U-notch tip than at the surface of the specimen. Thus, the difference in the strain concentration in the thickness direction revealed by the

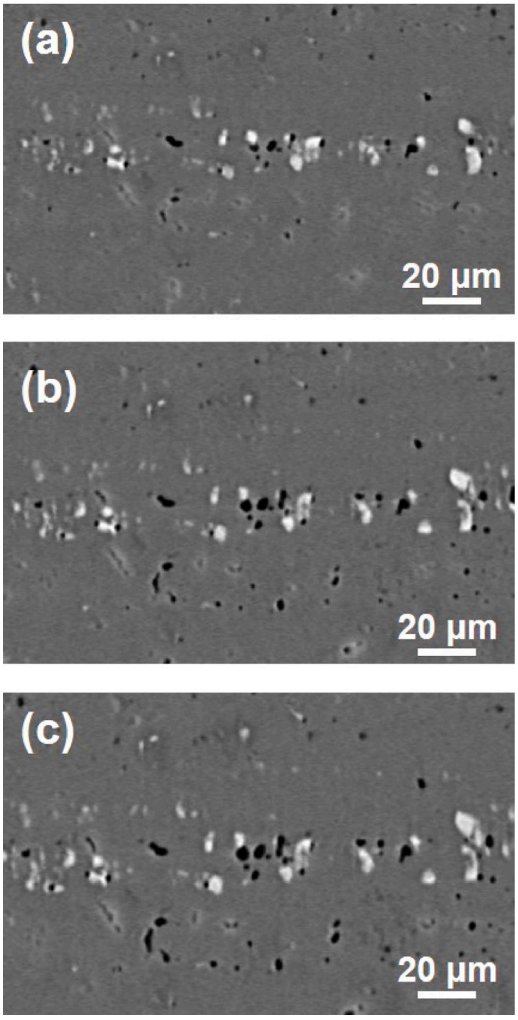

Fig. 8. Magnified images of the square part in Fig. 5: (a) unloading; (b) 400-N loading; (c) 600-N loading.

present calculation represents the strain concentration due to partial plastic constraint effects. From the figure, both tension and compression along x_3 around the notch occurred because of the loading setup. In the present loading setup, we used a self-made tensile testing apparatus in which one side of the jig was fixed and only the opposite side of the jig was allowed to operate. As the loading direction was unidirectional, polarity was expected to appear in the ε_{33} strain—particularly at the notch bottom perpendicular to the loading direction.

Surface compression along x_2 (negative ε_{22}) was also observed, although there was no significant internal compression. Owing to the Poisson effect caused by tensile loading in the x_3 direction, compression occurred in the x_1 and x_2 directions. It is speculated that compared with the compression strain in the x_1 direction, that in the x_2 direction is more significantly influenced by differences in the effective length in the direction of action and the preferential orientation of dispersed particles in the x_1 direction. Additionally, plastic zones are formed at the notch tip owing to the loading in the x_3 direction. The dimensions of these plastic zones are smaller in the central interior of the notch and increase as they approach the surface (in the x_2 direction) [31]. It is presumed that differences in the magnitude of the compression strain in the x_2 direction may arise because of the change in the state of the plastic zones between the surface and interior. A high Mises strain $\varepsilon_{\text{mises}}$ is observed at the surface and around the notch, indicating that plastic deformation usually occurs there. This is related to the aforementioned strain condition.

In the region around $(x_1, x_3) = (300, 300)$ in the center of the sample, a high strain concentration was observed (see the map of $\varepsilon_{\text{mises}}$ for 400 N and those of ε_{33} and $\varepsilon_{\text{mises}}$ for 600 N). To investigate the reason for this, magnified images corresponding to the strain map were examined, as shown in Fig. 8. In the region with a high strain concentration, the aggregation of particles and pores was observed. In contrast, the aggregation of such particles in the region around $(x_1, x_3) = (300, 300)$ at $x_2 = 400$ μm is not visible in the CT images, as shown in Fig. 9, which is consistent with the calculated strain maps. Thus, it is believed that these aggregations result in the detection of strain at the interface between the particles and the aluminum alloy; for example, the elastic interaction between the particles and pores causes the strain field [32]. We believe that the features of the calculated strain maps were reasonable.

5. Summary

We propose an approach for calculating the strain field inside materials using X-ray CT images during deformation tests. Our approach is based on the point matching of the detected impurities from the CT images, and each point in the reference and deformed CT images is used to construct a Voronoi diagram. In addition to the change in distance between the reference and deformed points, the volume and shape of the Voronoi polyhdra at each point are employed for point matching. Using the proposed method for a notched Al alloy sample, we calculated the change in the strain field around the notch in a tensile test using X-ray CT images obtained during deformation, and our method was validated. Once the strain field is calculated, we think it is possible to estimate the eigenstrains of the particles (inclusion) and gas pressure in the pore or blisters inversely using conventional micromechanics theory [33–35]. We plan to investigate this in future research.

CRediT authorship contribution statement

Akio Ishii: Conceptualization, Data curation, Formal analysis, Investigation, Methodology, Software, Validation, Visualization, Writing – original draft, Writing – review & editing. **Keitaro Horikawa:** Data curation, Formal analysis, Funding acquisition, Investigation, Resources, Validation, Writing – original draft, Writing – review & editing. **Masato Hoshino:** Resources. **Kentaro Uesugi:** Resources.

Declaration of competing interest

The authors declare that they have no known competing financial interests or personal relationships that could have appeared to influence the work reported in this paper.

Acknowledgments

This study was partially supported by a Grant-in-Aid for Scientific Research (C) 21K03771, (B)21H01604 from the Japan Society for the Promotion of Science (JSPS). This study was conducted under the General Proposal projects 2021B1143, 2022B1135, and 2023B1156 at the Japanese synchrotron facility SPring-8. K. H. acknowledges the partial financial support by The Light Metal Educational Foundation, Inc. in Osaka, Japan.

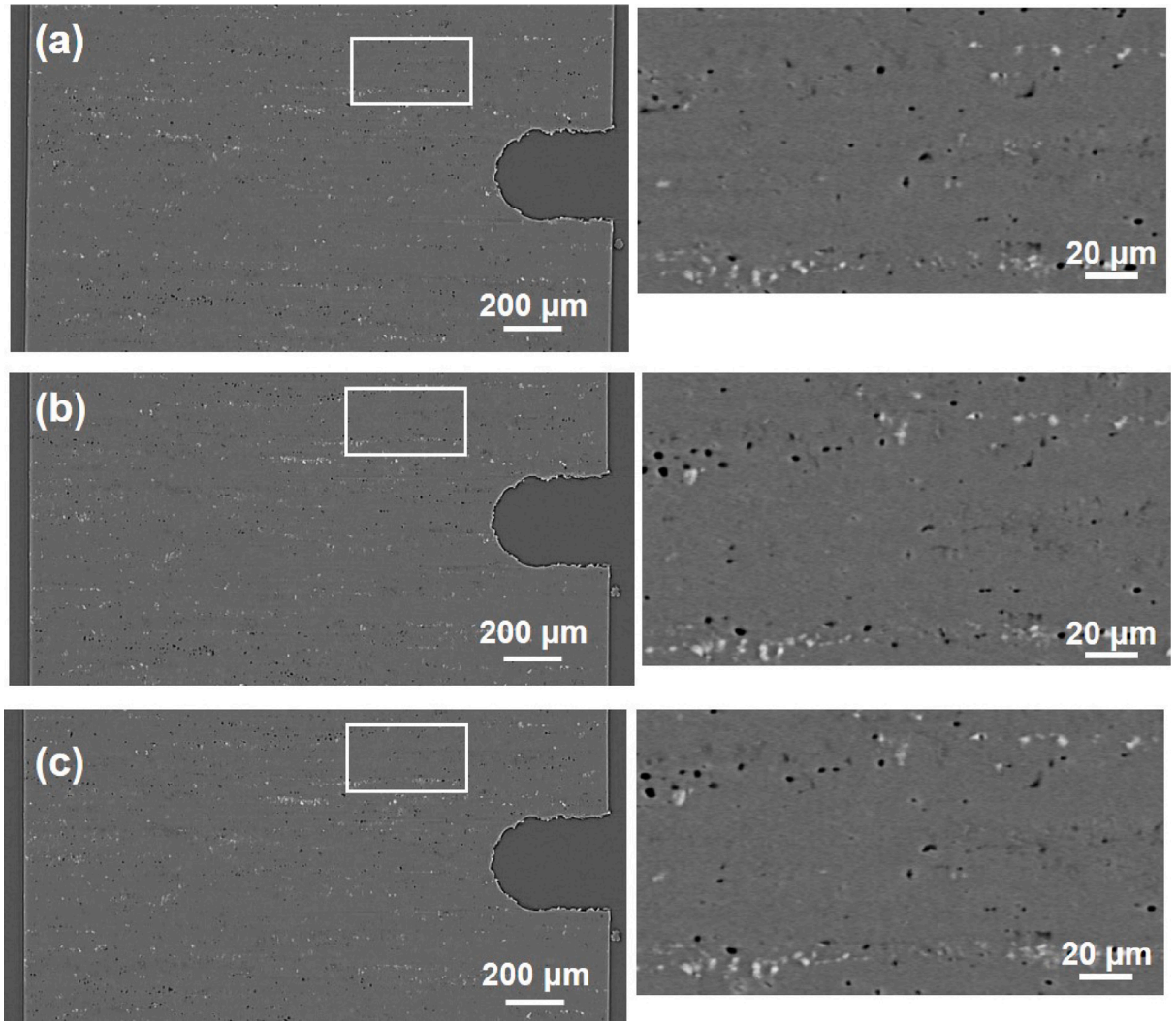

Fig. 9. X-ray CT images of the x_1–x_3 cross section around the notch at $x_2 = 400$ μm and magnified images of the square: (a) unloading; (b) 400-N loading; (c) 600-N loading.

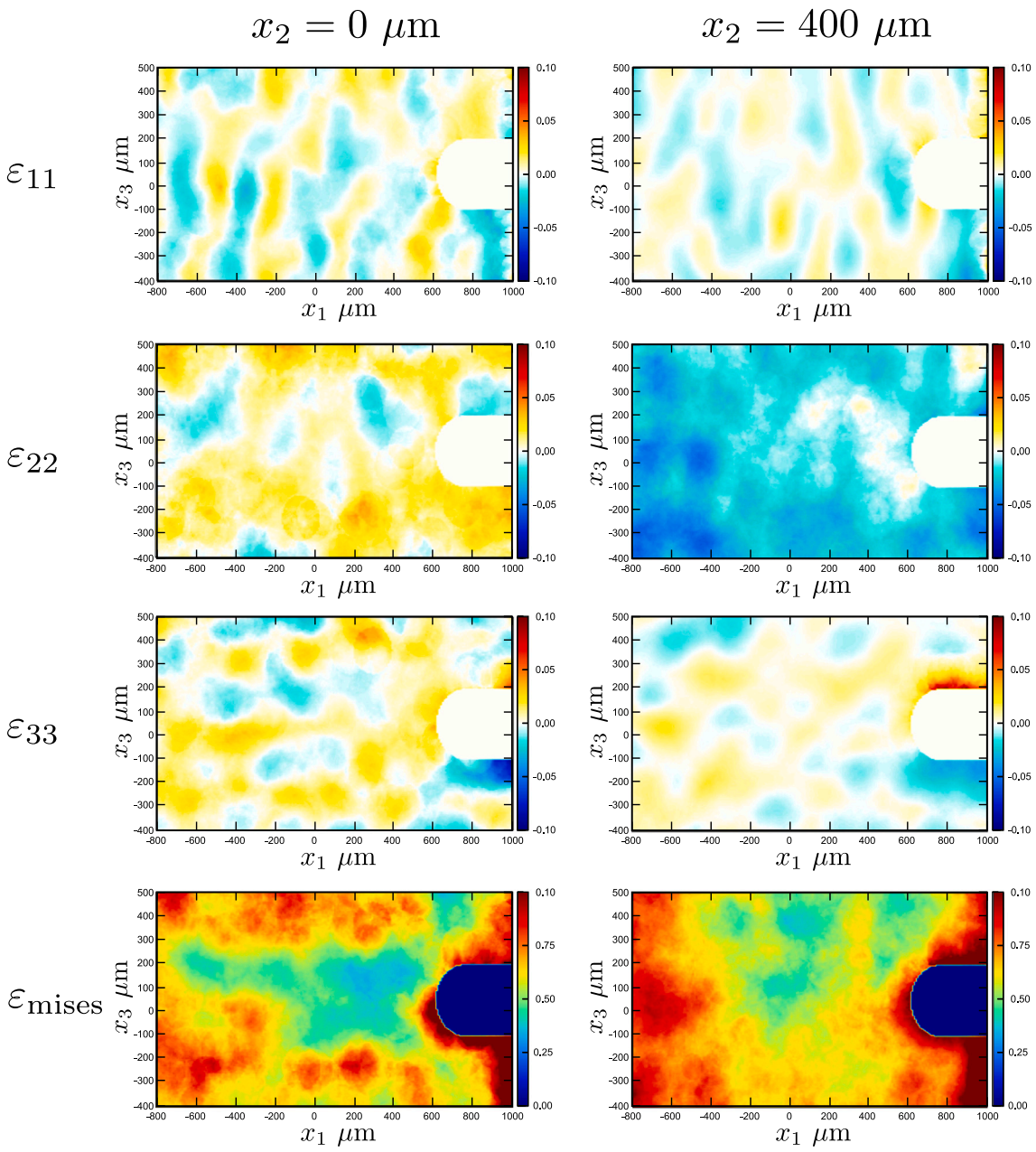

Fig. 10. Strain field around the notch for 400-N uniaxial tension calculated using the detected pores. The origin of the coordinate system is set at the center of mass of all the points.

Appendix. Strain-field calculation using pores

For comparison, we also calculated the strain field using the points of pores in unloading and the 400-N tension case with the same setting parameters as the matching. Through the thresholding of the CT images, 224241 and 222945 pores were detected as "dark" patterns for the unloading and 400-N tension conditions, and the calculated strain fields are presented in Fig. 10. We confirmed that the trend of the strain fields was almost identical to that of the particles, although the standard strain value generally increased, and the strain around the notch decreased. Although we cannot clearly confirm which strain field is more accurate, we believe that the particles are more credible because the pores in the samples sometimes vanish during deformation.

References

[1] K. Ueda, K. Horikawa, M. Kanno, Suppression of high temperature embrittlement of Al-5% Mg alloys containing a trace of sodium caused by antimony addition, Scr. Mater. 37 (1997) 1105–1110.
[2] H. Toda, I. Sinclair, J. Buffière, E. Maire, K.H. Khor, P. Gregson, T. Kobayashi, A 3D measurement procedure for internal local crack driving forces via synchrotron X-ray microtomography, Acta Mater. 52 (2004) 1305–1317.
[3] K. Horikawa, T. Matsubara, H. Kobayashi, Hydrogen charging of Al-Mg-Si-based alloys by friction in water and its effect on tensile properties, Mater. Sci. Eng. A 764 (2019) 138199.
[4] K. Horikawa, Quantitative monitoring of the environmental hydrogen embrittlement of Al-Zn-Mg-based aluminum alloys via dynamic hydrogen detection and digital image correlation, Scr. Mater. 199 (2021) 113853.
[5] M. Matsubara, R. Takara, T. Komatsu, S. Furuta, K. Pei Loon, M. Kobayashi, H. Mushiaki, K. Uesugi, S. Kawamura, D. Tajiri, In-situ measurement of dynamic micro X-ray CT and dynamic mechanical analysis for rubber materials, Mech. Syst. Signal Process. 205 (2023) 110875.
[6] F. Di Gioacchino, J. Quinta da Fonseca, Plastic strain mapping with sub-micron resolution using digital image correlation, Exp. Mech. 53 (2013) 743–754.

[7] J. Blaber, B. Adair, A. Antoniou, Ncorr: Open-source 2D digital image correlation matlab software, Exp. Mech. 55 (2015) 1105–1122.
[8] J. Stinville, N. Vanderesse, F. Bridier, P. Bocher, T. Pollock, High resolution mapping of strain localization near twin boundaries in a nickel-based superalloy, Acta Mater. 98 (2015) 29–42.
[9] J.C. Stinville, M.P. Echlin, D. Texier, F. Bridier, P. Bocher, T.M. Pollock, Sub-grain scale digital image correlation by electron microscopy for polycrystalline materials during elastic and plastic deformation, Exp. Mech. 56 (2016) 197–216.
[10] G. Tozzi, V. Danesi, M. Palanca, L. Cristofolini, Elastic full-field strain analysis and microdamage progression in the vertebral body from digital volume correlation, Strain 52 (2016) 446–455.
[11] R. Jiang, D. Bull, A. Evangelou, A. Harte, F. Pierron, I. Sinclair, M. Preuss, X. Hu, P. Reed, Strain accumulation and fatigue crack initiation at pores and carbides in a SX superalloy at room temperature, Inter. J. Fatig. 114 (2018) 22–33.
[12] J. Yang, L. Hazlett, A. Landauer, C. Franck, Augmented Lagrangian digital volume correlation (ALDVC), Exp. Mech. 60 (2020) 1205–1223.
[13] S. Nielsen, H. Poulsen, F. Beckmann, C. Thorning, J. Wert, Measurements of plastic displacement gradient components in three dimensions using marker particles and synchrotron X-ray absorption microtomography, Acta Mater. 51 (2003) 2407–2415.
[14] K. Haldrup, S.F. Nielsen, F. Beckmann, J.A. Wert, Inhomogeneous plastic flow investigated by X-ray absorption microtomography of an aluminium alloy containing marker particles, J. Micro. 222 (2006) 28–35.
[15] T. Ohgaki, H. Toda, M. Kobayashi, K. Uesugi, M. Niinomi, T. Akahori, T. Kobayash, K. Makii, Y. Aruga, In situ observations of compressive behaviour of aluminium foams by local tomography using high-resolution X-rays, Phil. Mag. 86 (2006) 4417–4438.
[16] M. Kobayashi, H. Toda, Y. Kawai, T. Kobayashi, K. Uesugi, D.S. Wilkinson, E. Maire, Y. Aoki, Measurement of 3-D strain distribution by means of high-resolution X-ray CT image and tracking of microstructural features, J. Japan Inst. Met. 71 (2007) 181–186 (in Japanese).
[17] K. Haldrup, S.F. Nielsen, J.A. Wert, A general methodology for full-field plastic strain measurements using X-ray absorption tomography and internal markers, Exp. Mech. 48 (2008) 199–211.
[18] K. Haldrup, F. Beckmann, S. Nielsen, J. Wert, Experimental determination of strain partitioning among individual grains in the bulk of an aluminium multicrystal, Mater. Charact. 59 (2008) 842–851.
[19] M. Kobayashi, Y. Zhang, H. Ishikawa, J. Sun, J. Oddershede, D.J. Jensen, H. Miura, Investigation of relationships between grain structure and inhomogeneous deformation by means of laboratory-based multimodal, Exp. Mech. 61 (2020) 817–828.
[20] M. Kobayashi, Y. Zhang, H. Ishikawa, J. Sun, J. Oddershede, D.J. Jensen, H. Miura, Relationships between 3D grain structure and local inhomogeneous deformation: A laboratory-based multimodal X-ray tomography investigation, Acta Mater. 240 (2022) 118357.
[21] E. Dall'Ara, M. Peña-Fernández, M. Palanca, M. Giorgi, L. Cristofolini, G. Tozzi, Precision of digital volume correlation approaches for strain analysis in bone imaged with micro-computed tomography at different dimensional levels, Front. Mater. 4 (2017).
[22] G. Tozzi, E. Dall'Ara, M. Palanca, M. Curto, F. Innocente, L. Cristofolini, Strain uncertainties from two digital volume correlation approaches in prophylactically augmented vertebrae: Local analysis on bone and cement-bone microstructures, J. Mech. Behav. Biomed. Mater. 67 (2017) 117–126.
[23] J.D. Bernal, A geometrical approach to the structure of liquids, Nature 183 (1959) 141–147.
[24] M. Wakeda, Y. Shibutani, S. Ogata, J. Park, Relationship between local geometrical factors and mechanical properties for Cu-Zr amorphous alloys, Intermetallics 15 (2007) 139–144.
[25] K.-W. Park, C.-M. Lee, M. Wakeda, Y. Shibutani, M.L. Falk, J.-C. Lee, Elastostatically induced structural disordering in amorphous alloys, Acta Mater. 56 (2008) 5440–5450.
[26] K.W. Park, C.M. Lee, M. Wakeda, Y. Shibutani, E. Fleury, J.C. Lee, Homogeneous deformation of bulk amorphous alloys during elastostatic compression and its packing density dependence, Scr. Mater. 59 (2008) 710–713.
[27] F. Shimizu, S. Ogata, J. Li, Theory of shear banding in metallic glasses and molecular dynamics calculations, Mater. Trans. 48 (2007) 2923–2927.
[28] C.H. Rycroft, G.S. Grest, J.W. Landry, M.Z. Bazant, Analysis of granular flow in a pebble-bed nuclear reactor, Phys. Rev. E 74 (2006) 021306.
[29] G. Chell, Developments in Fracture Mechanics. Vol. 1, Applied Science Publishers, 1979.
[30] M. Gupta, R. Alderliesten, R. Benedictus, A review of T-stress and its effects in fracture mechanics, Eng. Fract. Mech. 134 (2015) 218–241.
[31] D. Dugdale, Yielding of steel sheets containing slits, J. Mech. Phys. Soli. 8 (1960) 100–104.
[32] K. Horikawa, A. Ishii, Effect of purity on the internal morphology of blisters on aluminum surfaces, Res. Mater. 21 (2024) 100522.
[33] A. Ishii, *Ab* initio morphology prediction of Zr hydride precipitates using atomistically informed Eshelby's ellipsoidal inclusion, Comput. Mater. Sci. 211 (2022) 111500.
[34] A. Ishii, Influence of elastic anisotropy on the shapes of ellipsoidal blisters and stress field around the blisters in solid materials, AIP Adv. 13 (2023) 125024.
[35] A. Ishii, Morphology prediction of elastically interacting Zr hydride precipitates and cracks in α-Zr using atomistically informed Eshelby's ellipsoidal inclusion, Comput. Mater. Sci. 231 (2024) 112568.